Orientation-dependent two-dimensional magnonic crystal modes in an ultralow-damping ferrimagnetic waveguide containing repositioned hexagonal lattices of Cu disks

Kanta Mori,[1,2] Takumi Koguchi,[1] Toshiaki Watanabe,[3] Yuki Yoshihara,[1] Hibiki Miyashita,[1,2] Dirk Grundler,[4] Mitsuteru Inoue,[1] Kazushi Ishiyama,[1] and Taichi Goto[1,*]

[1] *Research Institute of Electrical Communication, Tohoku University, 2-1-1 Katahira, Aoba, Sendai, Miyagi, 980-8577, Japan*

[2] *Graduate School of Engineering, Tohoku University, 6-6 Aramaki, Aoba, Sendai, Miyagi, 980-8579, Japan*

[3] *Shin-Etsu Chemical Co., Ltd., 2-13-1 Isobe, Annaka, Gunma 379-0195, Japan*

[4] *Institute of Materials (IMX) and Institute of Electrical and Micro Engineering (IEM), Ecole Polytechnique Federale de Lausanne (EPFL), Lausanne, 1015, Switzerland*

(Received 21 November 2023; revised 21 December 2023; accepted 5 January 2024; published 30 January 2024)

Two-dimensional (2D) hexagonal lattices of Cu disks are shown to induce orientation-dependent magnonic crystal (MC) modes for propagating forward volume spin waves in a single-crystal yttrium iron garnet (YIG) film. The width and depth of the magnonic band gaps are 0.022 GHz and –15.2 dB at the frequency of 1.815 GHz. Integrating differently oriented lattices on the same YIG film and positioning them between the microwave antenna surrounded by magnon absorbers consisting of Au films, we clearly resolve a characteristic frequency shift of the magnonic band gap by altering the incident angle of the spin waves to the 2D MC. The shift amounts to approximately 10 MHz when the incident angle is changed between 10° and 30°. The obtained results show a good agreement with calculations using the finite integration technique and are a step toward complete band-gap investigations in YIG of ultralow spin-wave damping.

DOI: 10.1103/PhysRevApplied.21.014061

I. INTRODUCTION

Spin-wave (SW) logic devices [1–11] emerged as promising candidates for next-generation computing due to their minimal Joule heat generation and unique wave functionalities. A key to utilize these devices is controlling the propagation of SWs. This requirement has led to the study of a periodic magnetic structure, known as magnonic crystals (MCs) [12,13]. One-dimensional (1D) MCs were shown to exhibit magnonic band gaps (MBGs) theoretically [14–17] and experimentally [18–25]. They were applied in filtering [26], phase shifting [27], and SW confinement [28]. Two-dimensional (2D) MCs [13,29–33] have garnered further attention as they provide a complete magnonic band gap (CMBG) allowing for enhanced propagation control of SWs. Their characteristics position them as potential cornerstones for SW integrated circuits (IC), including logic gates [1,9,12]. To realize SW ICs, the forward volume spin wave (FVSW) is deemed suitable due to its in-plane isotropy, which is beneficial for guiding SWs [1,2,6,22,30,33,34]. Furthermore, ferrimagnetic yttrium iron garnet (YIG) is considered an optimal material for SW waveguides in SW ICs, owing to its extended SW propagation lengths attributed to a low-damping constant [1–6,34,35]. Notably, Chi *et al*. experimentally demonstrated 2D MCs using FVSWs propagating through a YIG waveguide with periodic grooves [29,30]. Validating the MBG of 2D MCs necessitates measuring its dependence on the incident angle. However, the MBG was observed at only a single SW incident angle [30]. This limitation is believed to arise from spectral oscillations and/or noise caused by multiple reflections of FVSWs at the edges of the waveguide and/or periodic structures, complicating the MBG observation in ultralow-damping YIG [22,36]. In this study, we have overcome this limitation by introducing SW absorbers composed of Au films positioned next to the microwave antenna on the YIG film. The suppressed edge reflections of FVSW allowed us to measure the incident angle dependence of the MBG of 2D MCs. The MCs were created using a carefully designed hexagonal lattice

*taichi.goto.a6@tohoku.ac.jp

of Cu disks, fabricated at different rotation angles on the same YIG film.

II. DESIGN OF 2D MC

A. Calculation model and conditions

The 2D MCs were designed using a simulator (CST Studio Suite 2022 SP5) based on the three-dimensional (3D) finite integration technique (FIT) [37, 38] because of the good agreement between calculation and experiment in previous studies on magnonic devices [1,22]. The 3D model of our sample is shown in Fig. 1. A 15 mm × 15 mm × 13 μm YIG film was located on two microstrip lines (MSLs) fabricated on a 170 × 170 × 1 mm^3 dielectric substrate (Isola, FR402) as shown in Fig. 1(a). The material parameters of the YIG were determined as single-crystal bulk values as shown in Table I, as follows: the saturation magnetization $4\pi M_s = 1800$ G [39], the relative permittivity $\varepsilon_{YIG} = 15.3$ [1], gyromagnetic ratio $\gamma = 2.8$ MHz/Oe [40], Gilbert damping $\alpha = 7 \times 10^{-4}$ [22]. The magnetic field was uniformly applied perpendicular to the YIG film. The internal magnetic field H_{in} was set as 600 Oe. The relative permittivity of FR4 was $\varepsilon_{FR4} = 4.4$. The width of the MSL was 60 μm. The thicknesses of the MSL and the GND plane formed on the back side of the dielectric substrate were 70 μm [Fig. 1(c)]. The MSL and the GND plane were composed of Cu with the conductivity of $\sigma_{Cu} = 5 \times 10^7$ S/m [41]. The length of the section with a 60-μm-wide MSL was 8.85 mm. The center-to-center distance between the two MSLs was 6.41 mm. The MSLs were in contact with the YIG film, but they did not touch the periodic Cu disks and SW absorbers composed of Au as shown in Fig. 1(c). The rf signals were input and output through these MSLs. The input power of the rf signal was set as 0.5 W to excite linear dipole SWs in the YIG waveguide [42]. The impedance of the input and output ports used in the calculation was set to 50 Ω. The shortest length of one side of the tetragonal mesh in this model was 3 μm.

TABLE I. Physical constants and structural features used in the calculations, along with their measured values.

Parameter	Calculation	Experiment
YIG thickness, t_{YIG}	13.0 μm	10.7 μm
YIG saturation magnetization, $4\pi M_s$	1800 G	1732 G
YIG internal magnetic field, H_{in}	600 Oe	603 Oe
Cu disk thickness	1.0 μm	1.1 μm
Cu disk diameter, d	300.0 μm	301.2 μm
Air gap between Cu disks	150.0 μm	146.3 μm
Lattice constant, a	450.0 μm	447.5 μm
MSL width	60.0 μm	62.1 μm
Air gap between MC-MSL, g_{MC-MSL}	20.0 μm	23.4 μm
Air gap between MSL-Au, g_{MSL-Au}	10.0 μm	9.9 μm
Au thickness	30.0 nm	42.4 nm

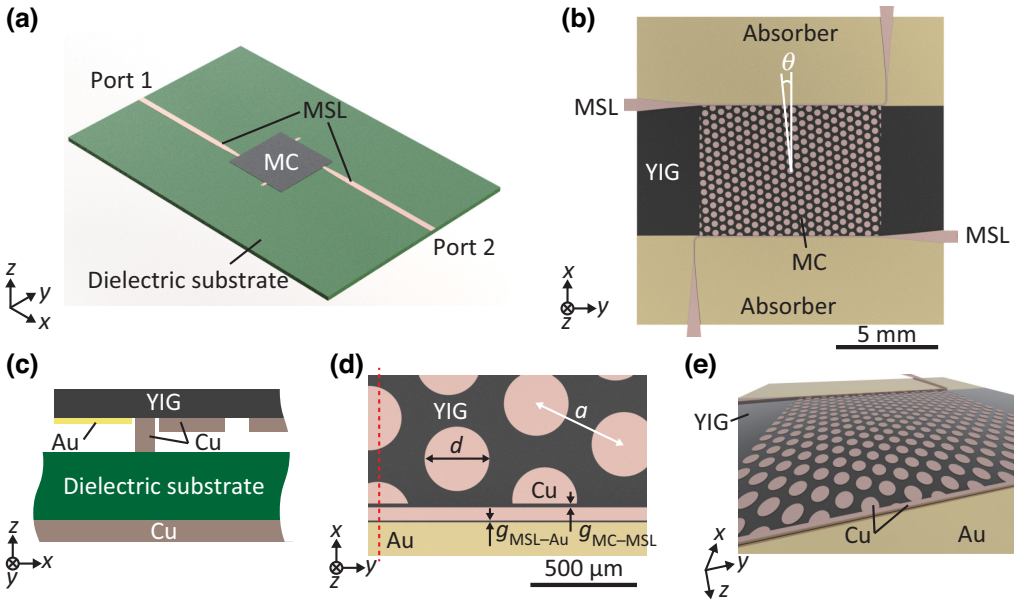

FIG. 1. (a) Sketch of the 2D MC flip chipped onto the MSL in contact with the dielectric substrate. (b) Bottom view of the YIG film with the MC consisting of Cu disks, and the MSL in contact with the YIG film. The MC is tilted at an angle θ. (c) Cross-section sketch of the 3D model cut along the red dashed line shown in (d). (d) Enlarged view of the area near the edge of the MC and MSL from (b). (e) Bird's eye view of (b).

Periodic Cu disks were placed hexagonally on the YIG surface between the two MSLs. The diameter and periodicity of Cu disks were determined using calculated dispersion curves. The wavelength λ_{YIG} of the FVSW propagating in the infinite YIG film can be expressed as the following equation [39]:

$$\lambda_{YIG} = 2\pi t_{YIG}\sqrt{\mu}\left\{\ln\left(\frac{\sqrt{\mu}-1}{\sqrt{\mu}+1}\right)\right\}^{-1}, \quad (1)$$

where t_{YIG} is the YIG thickness and μ is expressed as the following equation [22,42]

$$\mu = 1 + \frac{(\gamma H_{in} + i\alpha f)(\gamma \times 4\pi M_s)}{(\gamma H_{in} + i\alpha f)^2 - f^2}, \quad (2)$$

where f is the frequency. The wavelength $\lambda_{Cu/YIG}$ of SWs in an infinite Cu-covered YIG film is expressed as the following equation [39]:

$$\lambda_{Cu/YIG} = 4\pi t_{YIG}\sqrt{\mu}\left\{\ln\left(\frac{\sqrt{\mu}-1}{\sqrt{\mu}+1}\right)\right\}^{-1} = 2\lambda_{YIG}. \quad (3)$$

The wavelength of the SW propagating in the Cu-covered YIG is twice as large as that in the uncovered YIG due to the difference in surface boundary conditions. Using Eqs. (1) and (3), we determined the diameters of the Cu disks d to be $\lambda_{Cu/YIG}/4$ and the air gaps between the Cu disks to be $\lambda_{YIG}/4$, the same as in 1D MC [22]. We set the value of λ_{YIG} to 600 μm to clearly observe the MBG in the high transmission spectra; consequently, the diameter of the Cu disks was 300 μm, the air gap between them was 150 μm, and the periodicity (lattice constant) a of the 2D MC was 450 μm [Fig. 1(d)]. The thickness of Cu disks was set to 1 μm, based on previous report indicating this thickness to be sufficient for modulating SW properties [43]. These Cu disks were not in contact with the dielectric substrate as shown in Fig. 1(c). We investigated differently rotated lattices of Cu disks, which led to 2D MC tilted under different angles θ to the MSL, as shown in Fig. 1(b). Thereby we obtained the incident angle dependence of the SW propagation through nominally identical Cu disk lattices.

The SW absorbers, consisting of 30-nm-thick Au with a conductivity σ_{Au} of 4.56×10^7 S/m [41], were placed at the edges of the YIG waveguide to suppress the SW reflection. The air gap between the edges of the MCs and the MSL g_{MC-MSL} was 20 μm, and the air gap between the MSL and the SW absorber g_{MSL-Au} was 10 μm, as shown in Fig. 1(d). These gaps were determined to be sufficiently smaller than the wavelength of the SWs to avoid generating transmission spectral ripple and notch due to the SW standing-wave mode between the MSL-MC and MSL-Au [36].

B. Calculation results

The transmission spectra S_{21} of SWs at various incident angles θ, ranging from 0° to 30° relative to the 2D MC, were calculated by rotating the MCs on the YIG film, as shown in Fig. 2(a). Figures 2(b) and 2(c) show the calculated results (blue curves) for the intensity and the real part of the S_{21} spectra, respectively. In the top sample of Fig. 2, the absence of Cu disks resulted in a flat SW transmission spectrum without any MBG. After forming a MC by inserting the Cu disks onto the YIG film, the MBG remained unobservable for SW incident angles of $\theta = 0°$ and 5° due to its overlap with the SW attenuation range, which was prominent for frequencies $f > 1.825$ GHz.

Increasing the SW incident angle to 10° or higher caused the MBG to shift to the lower-frequency side, enabling the observation of the MBG in the blue curves (upward black triangle). The phase shift shown in Fig. 2(c) confirms the presence of the MBG (highlighted by an upward triangle), distinguishing it from spectral ripple or typical interference fringes.

The calculated transmission spectra are represented as color maps in Figs. 3(a) and 3(c). Figure 3(a) features a bright blue region indicating the propagation of SWs, mirrored by a distinct striped region in Fig. 3(c). The propagation region's lowest frequency, 1.68 GHz, matches the ferromagnetic resonance (FMR) frequency of the YIG, denoted as f_{FMR} $(=\gamma H_{in})$. Two MBGs were observed: the first MBG had a narrow bandwidth, exhibited around 1.815 GHz, and shifted to a lower frequency with increasing incident angle θ. The second MBG, with a wider bandwidth, was observed between approximately 1.83 GHz and approximately 1.92 GHz, and shifted to a higher frequency as the incident angle θ increased.

III. EXPERIMENT

A. 2D MC fabrication

The 2D MCs designed for various SW incident angles, as shown in Fig. 2(a), were fabricated using the lithography technique depicted in Figs. 4(a)–4(g).

Figure 4(a) illustrates a 10.7-μm-thick YIG film on a $15 \times 15 \times 0.5$ mm^3 gadolinium gallium garnet (GGG) substrate. The YIG was epitaxially grown on both sides of the GGG substrate using the liquid phase epitaxial (LPE) method at a temperature of approximately 900 °C, and subsequently, one side of the YIG was removed by chemical mechanical polishing (CMP). The GGG substrate was (111) oriented with a deviation of ±0.1° and had a lattice constant of 1.2383 ± 0.0001 nm. The YIG, also a (111)-oriented single crystal, featured optically polished surfaces. The lattice mismatch between the YIG and the GGG substrate was under 0.03%. The growth speed was 0.4 μm/min. The FMR linewidth ΔH of the YIG was 0.67 Oe at an applied field H_0 of 4630 ± 10 Oe and at a

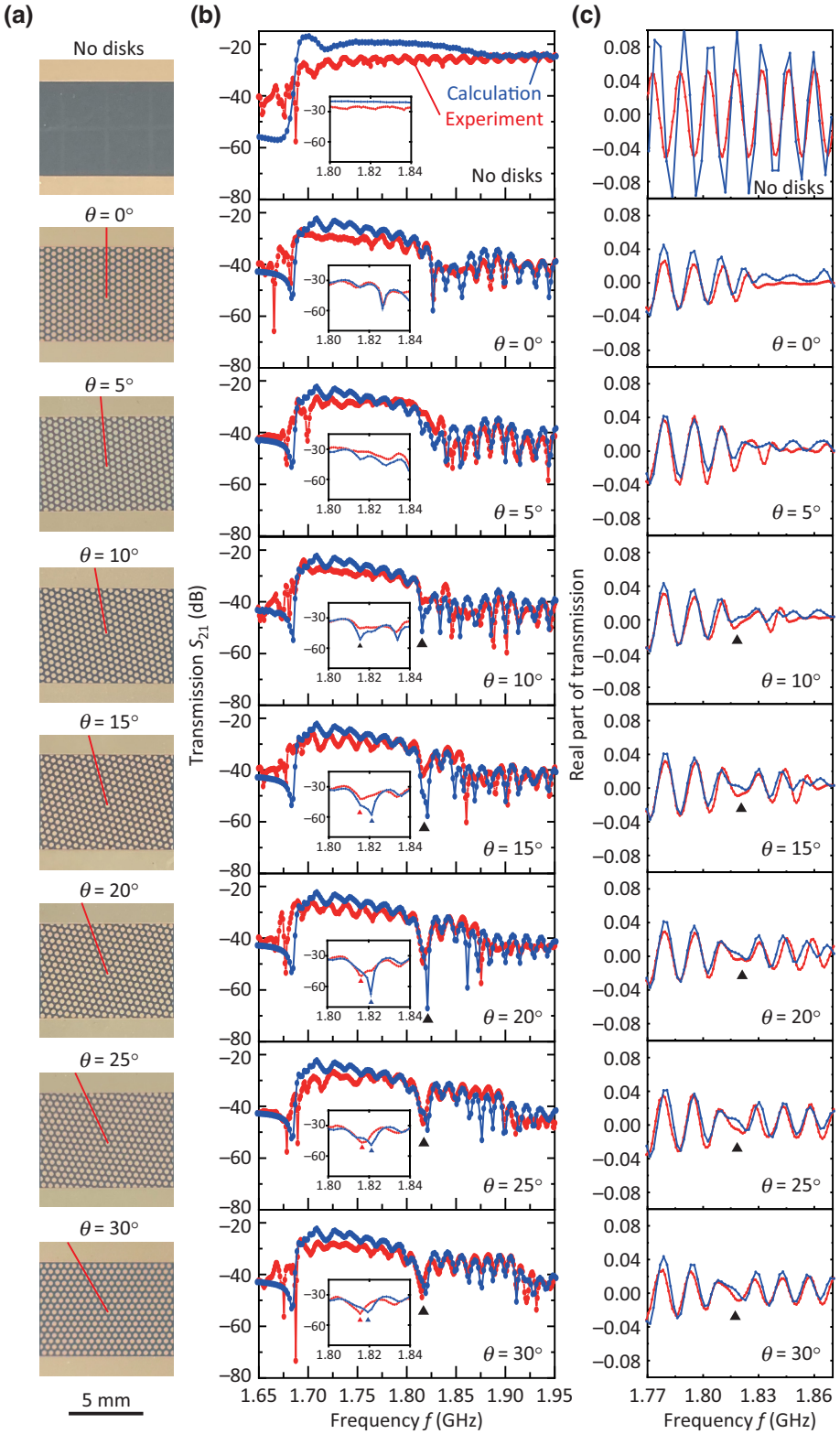

FIG. 2. (a) Photos of the top view of the fabricated 2D MCs with a tilting angle θ relative to the SW incident direction, like calculation models. (b) Transmission S_{21} spectra through the 2D MC. (c) Real part of the S_{21} spectra. Red and blue plots correspond to experimental and calculated results, respectively, with triangles indicating the spectral positions of MBGs.

temperature of 25.9 °C. The YIG thickness was determined from a cross-section image obtained by a focused-ion beam and scanning electron microscope system (FIB-SEM, FEI Versa 3D).

Figure 4(b) shows the Cu deposition step. A 1.1-μm-thick Cu film was deposited on the YIG film by direct-current ion beam sputtering (dc IBS, TDY, 98012-RD). The base pressure of the vacuum chamber was maintained

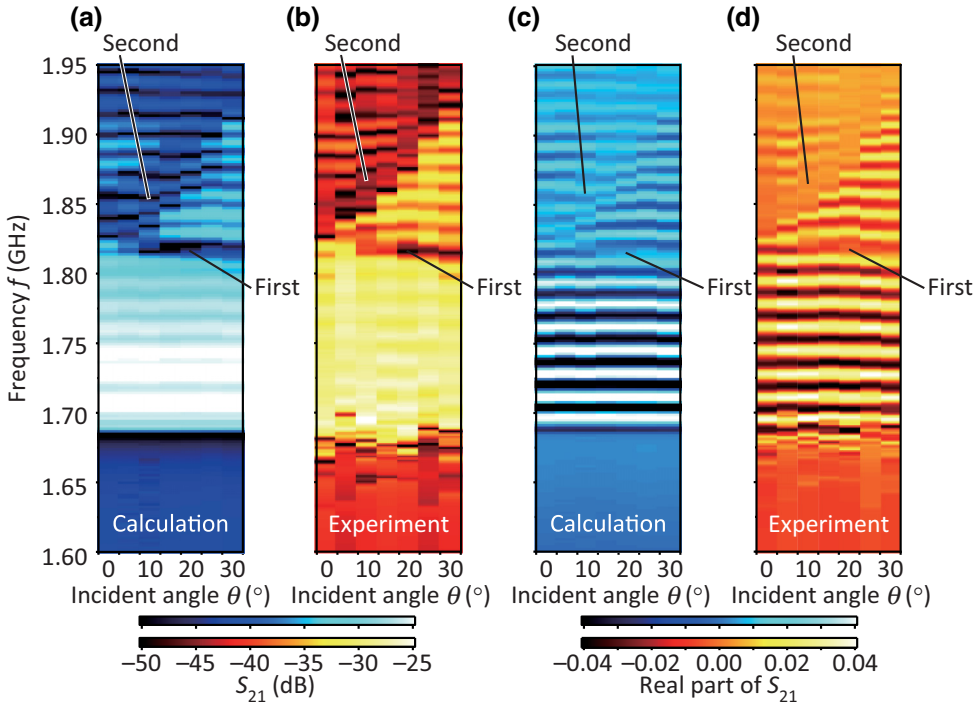

FIG. 3. SW incident angle θ dependence for 2D MCs: (a),(b) transmission S_{21} spectra and (c),(d) their real part. (a),(c) show calculated and (b),(d) show measured results.

at 7×10^{-7} Torr. The Ar gas flow was set to 5 sccm for the sputter gun and 4 sccm for the neutralizer. Deposition was conducted at 2.4×10^{-4} Torr using a Furuchi Chemical No. 19002130 Cu target, with a beam current of 27 mA and a deposition rate of 8.46 nm/min. The smoothness of the Cu film surface was verified by a SEM (Hitachi High-Tech, SU6600) image presented in Fig. S1 within the Supplemental Material [44].

Figure 4(c) shows the fabrication of the patterned mask. The sample was baked at 100 °C for 5 min to eliminate moisture before a 1.76-μm-thick layer of photoresist AZ5214E was spin coated onto it. Subsequent baking at 110 °C for 50 s preceded exposure to a dose of 110 mJ/cm^2 with a maskless aligner (Heidelberg Instruments, μMLA). A reversal bake at 120 °C for 2 min and a 2.5-min full exposure were followed by a 1-min development in a solution of AZ400K:H_2O at a 1:5 ratio.

Figure 4(d) shows the fabrication of the Cu disks and MSLs. The Cu uncovered by resist was etched by immersing the sample in $FeCl_3$ for 25 s. Subsequent to etching, the remaining resist was stripped away by immersion in AZ700 remover for 5 min, followed by cleaning with acetone and isopropyl alcohol (IPA) without sonication.

Figure 4(e) shows the fabrication of the SW absorbers comprising Au films near the MSLs. The lithography procedure was repeated with a change in deposition material from Cu to Au, using a cross-shaped alignment mark for patterning the Au. The sample was baked at 100 °C for 5 min to eliminate moisture. Then, a 1.76-μm-thick layer of the same photoresist AZ5214E was spin coated on it, followed by baking at 110 °C for 50 s again. The sample was exposed to a dose of 160 mJ/cm^2 using the same maskless aligner, followed by a 1-min development in a solution AZ400K:H_2O at a 1:4 ratio. A 42.4-nm-thick Au was then deposited on the sample using dc IBS with the same condition, as depicted in Fig. 4(f). After liftoff, the resist using acetone without sonication, the sample was cleaned with acetone and IPA without sonication. Finally, the designed 2D MC was fabricated as shown in Figs. 4(g), 4(i), and 4(j). The fabricated Cu disks had a diameter of 301.2 μm, air gap between the Cu disks was 146.3 μm, and the width of the MSL was 62.1 μm, as observed by a microscope. The gaps between the MC-MSL and MSL-Au were 23.4 and 9.9 μm, respectively. Consequently, the structural difference of the fabricated sample from the design was $<17\%$, primarily attributable to the alignment error between the Cu and Au layers.

B. Measurement of SW transmission

The sample was placed on a $170 \times 170 \times 0.6$ mm^3 dielectric substrate featuring two electrically open MSLs, as shown in Fig. 4(k). These MSLs and the GND plane on the back side of the dielectric substrate consisted of 70-μm-thick Cu. The MSLs on the sample were electrically connected to those on the dielectric substrate

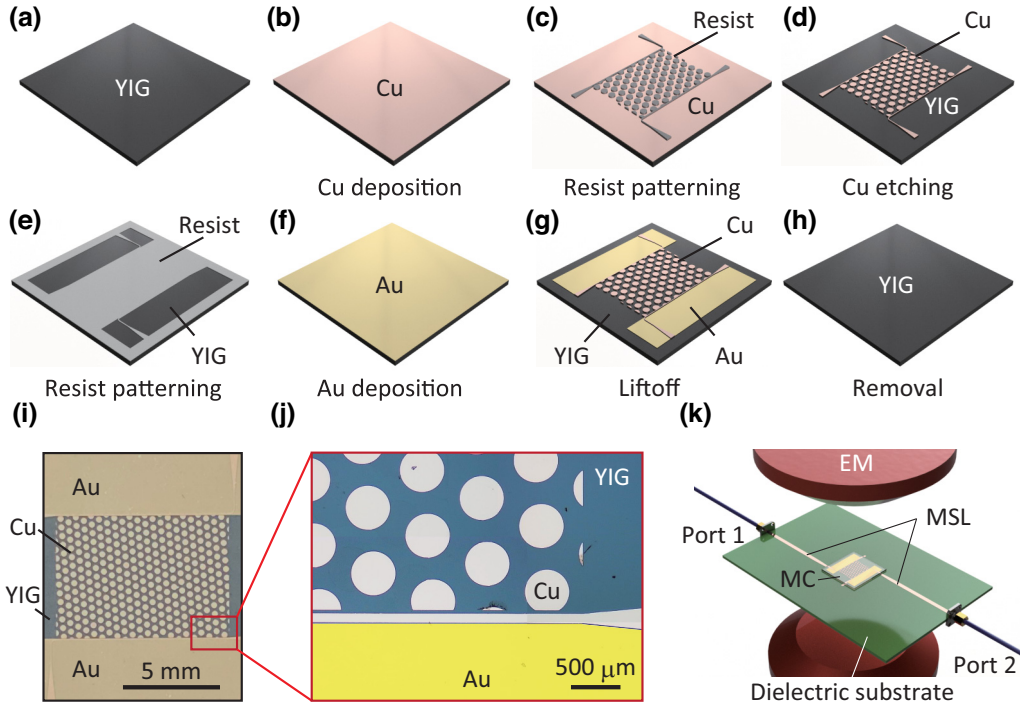

FIG. 4. Process for preparing the 2D MC samples. (a) Single-crystal YIG was grown on a GGG substrate. (b) Cu was deposited. (c) Photoresist was patterned using a maskless aligner. (d) Cu uncovered by photoresist was etched. (e) Photoresist was exposed again for SW absorber fabrication. (f) Au was deposited. (g) Photoresist was lifted off. (h) All metal on the YIG was removed. (i) Photo of the fabricated sample with an SW incident angle θ of 5° and (j) an enlarged image of the area near the MSL and SW absorber. (k) Overview of the measurement setup. Transmission spectra were measured by the VNA while a magnetic field was applied perpendicular to the sample using an EM.

through flip-chip bonding. The sample was fixed on the dielectric substrate using tape to prevent displacement of the contact position when a magnetic field was applied. A 5-mm-thick acrylic plate was placed on top of the sample and tightened using nonmagnetic screws at a torque of 5 N cm to ensure the electrical connection. The SMA connectors soldered to the MSLs on the dielectric substrate were connected to a vector network analyzer (VNA, Keysight Technologies, E5071C) via coaxial cables. This setup was placed within an electromagnet (EM, Toei Kagaku Sangyo, TKSJ-V500-TYP).

Before the measurement, the VNA was calibrated using an electronic calibration kit (Keysight Technologies, N4433A). The transmission S_{21} spectra were measured while applying a perpendicular magnetic field H_0 to the sample plane using the EM. Measurements were conducted in the frequency f range of 300 kHz to 8 GHz with 1-MHz steps and in the magnetic field H_0 range of –4 to 4 kOe with 5 Oe steps.

After all characterizations, the sample was removed from the measurement setup, and all metal components (Cu disks, MSLs, and Au SW absorbers) were stripped from the YIG film as shown in Fig. 4(h), in preparation for subsequent experiment using tilted Cu disk lattices on the same YIG film. The reason for repeatedly using the same YIG film rather than different ones, lies in the technical difficulties associated with fabricating multiple 15-mm square YIG films of identical thickness. Even minimal variations in thickness can modify the SW dispersion relation and, simultaneously, change the spectral position of the MBG. Hence, we opted to reuse the same YIG film for consistency. The metals were removed by immersing in an aqua regia solution of HNO_3:HCl at a 1:3 ratio for 5 min, followed by cleaning the samples using acetone and IPA with sonication. Subsequently, Cu disks at different SW incident angles θ, the same Cu MSLs, and the same Au SW absorbers were fabricated using the same fabrication process on the same YIG-GGG substrate, followed by the same measurements. We repeated these fabrication and measurement cycles 7 times to obtain the SW incident angle dependence of the transmission S_{21} spectra using the same YIG film.

C. Experimental results

Figure 5(a) shows the transmission spectra at a SW incident angle θ of 30°. Results for other angles are presented in Fig. S2 within the Supplemental Material [44]. The measured data was obtained at an applied field H_0 of –2335 Oe corresponding to an internal field H_{in}=–603 Oe

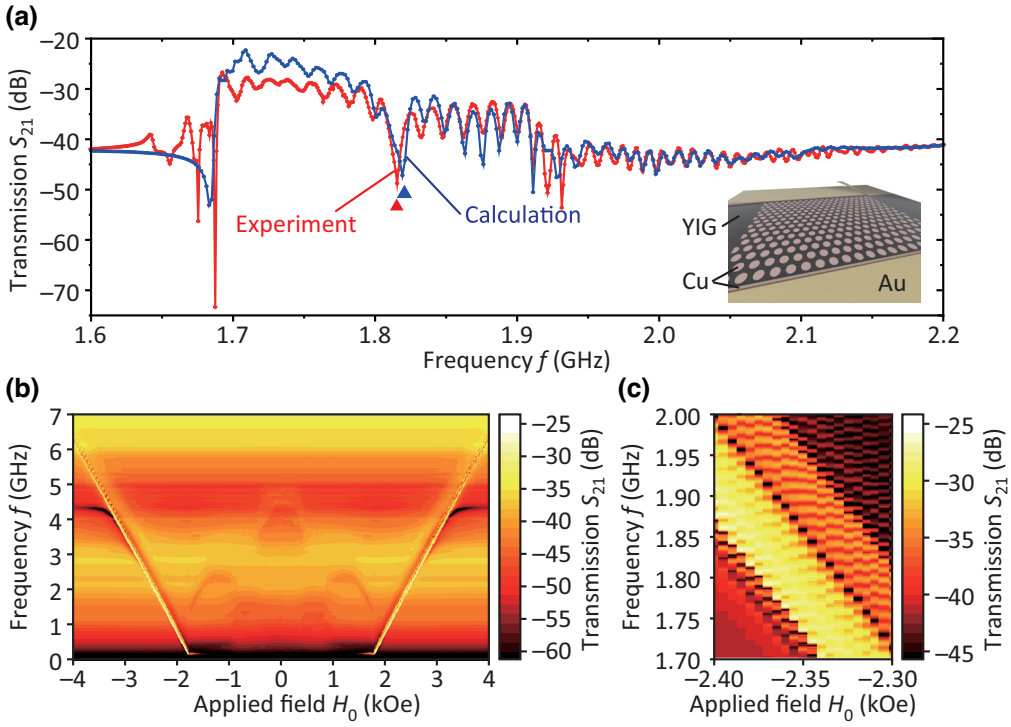

FIG. 5. Transmission S_{21} spectra measured at an SW incident angle θ of 30° (a) Measured transmission S_{21} spectrum (red) of MC at an applied field H_0 of –2335 Oe and the corresponding calculated spectrum (blue). (b) SW spectroscopy results showing SW propagation curves. (c) Detailed view of (b) highlighting the MBG shift.

$(=H_0 + 4\pi M_s = -2335 + 1732$ Oe), with the saturation magnetization $4\pi M_s$ measured by a vibrating sample magnetometer (VSM, Tamakawa TM-VSM2050-HGC-TOH) as shown in Fig. S3 within Supplemental Material [44]. The calculation was conducted for an internal field H_{in} of 600 Oe. The MBG was generated at a frequency f of approximately 1.815 GHz, showing a good agreement to the measured data. These MBGs were much clearer than that in previous reports [29,30] because of the SW absorber and the flat YIG waveguide. Consequently, we obtained a color map by measuring the spectra at various applied field, as shown in Figs. 5(b) and 5(c). Symmetric SW branches were observed between positive and negative applied fields [22,34]. The x intercepts of both curves were at $H_0 = 1732$ Oe, corresponding to the magnetic anisotropy field of the YIG film. The predominant magnetic anisotropy was the shape anisotropy, $4\pi M_s$ (=1732 Oe). Thus, the curves were fitted with the equation like (Kittel formalism):

$$f = \pm\gamma(H_0 \mp 4\pi M_s). \tag{4}$$

In Fig. 5(c), the MBG was represented by black dots within the yellow region, shifting in accordance with the same slope of Eq. (4). This consistency validated the observed MBG as a genuine feature of the fabricated 2D MC, not measurement noise.

IV. DISCUSSION

A. SW incident angle dependence

Figure 2(b) shows lineplots of calculated (blue) and measured spectra (red) for different incident angles θ. Figure 3 depicts corresponding color maps. A frequency drift during measurements was calibrated using the fourth positive peak in real-part sine curve signals shown in Fig. 2(c). Both the first and second MBGs predicted by calculations were observed in experiments. Their SW incident angle dependences show good agreement between experiment and calculations. A slight discrepancy was observed in the measured spectral position of the first MBG at $\theta = 30°$. It exhibited at a frequency of 1.815 GHz in the experiment, while the calculated value was 1.819 GHz. Such a variance is likely due to the mismatch of physical parameters, including material inhomogeneity and variations, and the modeling mesh-size limitation in the 3D simulation. The structural imperfections were not the primary cause of the spectral discrepancy between the experiment and calculation, validated by further simulations, detailed in Fig. S4 and Table S1 within the Supplemental Material [44].

The spectral positions f_{MBG} of the calculated and measured first MBG are plotted versus SW incident angle in Fig. 6. To depict the width of the MBG, the low- and high-frequency edges were also plotted. (The procedure to

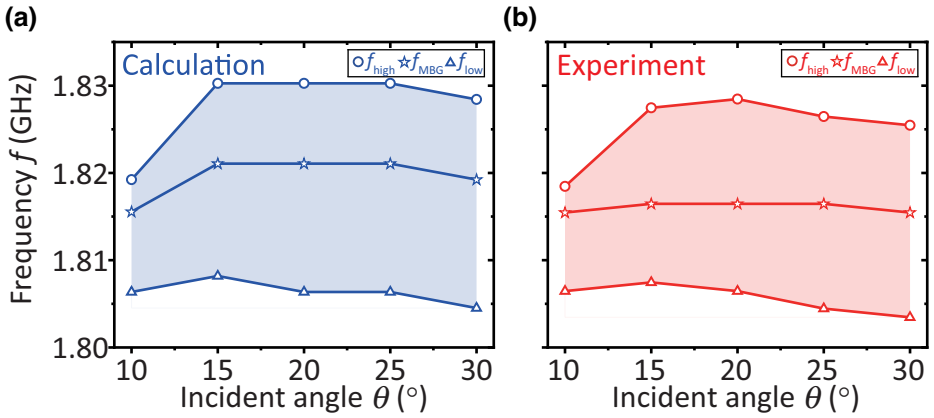

FIG. 6. SW incident angle dependence of the first MBG in (a) calculations and (b) experiments. Triangles and circles indicate the low-frequency edge f_{low} and high-frequency edge $f_{high,}$ of the MBG. Stars indicate the spectral position f_{MBG} of the MBG.

determine these frequencies is described in the Supplemental Material [44] with Fig. S5.) The spectral position f_{MBG} of the first MBG was slightly shifted at $\theta > 10°$, similar to the optical responses of hexagonal-aligned photonic crystals [45]. Such a tendency has not been clearly obtained with experimental results so far, validating the benefits of the SW absorber and periodic Cu disks used in the present work.

B. SW attenuation at the high-frequency region

The transmission spectra did not exhibit MBGs at SW incident angles between $\theta = 0°$ and 10° in Figs. 2(b) and 3 due to SW attenuation attributed to eddy current losses in the Cu disks. The skin depth of the Cu disks was 1.7 μm, calculated with a Cu conductivity σ_{Cu} of 5×10^7 S/m at a frequency f of 1.825 GHz, exceeding the thickness of Cu disks [46]. Hence, using Cu disks thicker than 1.7 μm could suppress the eddy currents. Furthermore, increasing the boundary using a multilayer structure with different metals is a promising approach to reduce eddy currents and enhance transmission in the high-frequency range.

C. Comparison

Even with the elimination of SW attenuation, the fabricated 2D MC could not exhibit a CMBG reflecting the SW at all incident angles. As shown in Figs. 3(a), 3(b), and 6, at a frequency f of 1.815 GHz, the spectral position of the first MBG between $\theta = 10°$ and 30° remained almost constant; however, it shifted to the higher frequency side between 0° and 5°. The shift is larger than the MBG's width of approximately 10 MHz. This behavior was consistent in both calculations and experiments, indicating that this 2D MC cannot inherently exhibit CMBG.

Chi *et al.* predicted the CMBG generation for FVSW using a square-aligned grooves on YIG [29,30]. Three band structures exhibiting CMBGs at frequencies of 8.49, 8.85, and 9.28 GHz were calculated, each with a bandwidth of <10 MHz. Krawczyk *et al.* anticipated a CMBG for FVSW using a square-aligned antidot pattern in a 41-nm-thick Co-Fe-B film [13]. They predicted a forbidden frequency gap across all SW incident angles with a bandwidth of 0.5 GHz when the hole diameter was 240 nm. These theoretical works were based on square-aligned periodic structures. Our simulations and experiments now demonstrate that the hexagonal-aligned structure is also promising, providing a substantial MBG width of 0.022 GHz and clear in-plane anisotropy due to its hexagonal symmetry. Structural considerations for achieving CMBG for FVSW, including hexagonal alignment of Bragg scatterers, have not been widely reported. To explore CMBG in differently designed 2D MCs, the plane-wave method [47] could be effective to calculate band structures. Introducing an alternative structural lattice symmetry and unit cell size could open the path to a CMBG for FVSWs in micrometer-thick YIG.

V. CONCLUSION

The 2D MC consisting of Cu disks with a 301.2-μm diameter and a 146.3-μm spacing patterned on a 10.7-μm-thick single-crystal YIG film was fabricated between two 62.1-μm-wide MSLs adjacent to SW absorbers made of Au films. The SW incident angle dependence of the 2D MC showing MBG for FVSW was obtained, validated by calculations using FIT. Two MBGs were clearly observed within the range between 1.8 and 1.9 GHz. These MBGs were shifted as the SW incident angle increased, indicating the potential for further structural improvement of the 2D MC for achieving a CMBG for FVSWs in YIG. Consequently, this work represents a demonstration of incident angle dependence of an MBG for FVSW in YIG-based 2D MCs. We consider our experiments and findings to be the precursor and significant step toward a CMBG for SW control over macroscopic propagation lengths in YIG.

ACKNOWLEDGMENTS

This work was partly supported by the Japan Society for the Promotion of Science (JSPS) KAKENHI Grants No. 20H02593, No. 20K20535, No. 23H01439, and No. 23K17758; the New Energy and Industrial Technology Development Organization (NEDO) Grants No. 20002157-0, and No. 23200047-0, and the Inamori Foundation. K.M. thanks the Japan Science and Technology Agency (JST) SPRING No. JPMJSP2114. T.G. thanks the TI-FRIS fellowship. Y.Y. and T.K. thank the TUT-DC fellowship. D.G. thanks SNSF for support via Grant No. 197360. We also acknowledge the Center for Integrated Nanotechnology Support (CINTS), the Laboratory for Nanoelectronics and Spintronics (LNS), and the Fundamental Technology Center of Tohoku University (FTCTU).

[1] T. Goto, T. Yoshimoto, B. Iwamoto, K. Shimada, C. A. Ross, K. Sekiguchi, A. B. Granovsky, Y. Nakamura, H. Uchida, and M. Inoue, Three port logic gate using forward volume spin wave interference in a thin yttrium iron garnet film, Sci. Rep. **9**, 16472 (2019).

[2] N. Kanazawa, T. Goto, K. Sekiguchi, A. B. Granovsky, C. A. Ross, H. Takagi, Y. Nakamura, and M. Inoue, Demonstration of a robust magnonic spin wave interferometer, Sci. Rep. **6**, 30268 (2016).

[3] M. P. Kostylev, A. A. Serga, T. Schneider, B. Leven, and B. Hillebrands, Spin-wave logical gates, Appl. Phys. Lett. **87**, 153501 (2005).

[4] T. Schneider, A. A. Serga, B. Leven, B. Hillebrands, R. L. Stamps, and M. P. Kostylev, Realization of spin-wave logic gates, Appl. Phys. Lett. **92**, 022505 (2008).

[5] T. Fischer, M. Kewenig, D. A. Bozhko, A. A. Serga, I. I. Syvorotka, F. Ciubotaru, C. Adelmann, B. Hillebrands, and A. V. Chumak, Experimental prototype of a spin-wave majority gate, Appl. Phys. Lett. **110**, 152401 (2017).

[6] N. Kanazawa, T. Goto, K. Sekiguchi, A. B. Granovsky, C. A. Ross, H. Takagi, Y. Nakamura, H. Uchida, and M. Inoue, The role of Snell's law for a magnonic majority gate, Sci. Rep. **7**, 7898 (2017).

[7] K.-S. Lee and S.-K. Kim, Conceptual design of spin wave logic gates based on a Mach–Zehnder-type spin wave interferometer for universal logic functions, J. Appl. Phys. **104**, 053909 (2008).

[8] N. Sato, K. Sekiguchi, and Y. Nozaki, Electrical demonstration of spin-wave logic operation, Appl. Phys. Express **6**, 063001 (2013).

[9] A. B. Ustinov, E. Lähderanta, M. Inoue, and B. A. Kalinikos, Nonlinear spin-wave logic gates, IEEE Magn. Lett. **10**, 1 (2019).

[10] A. V. Chumak, *et al.*, Advances in magnetics roadmap on spin-wave computing, IEEE Trans. Magn. **58**, 1 (2022).

[11] A. A. Serga, A. V. Chumak, and B. Hillebrands, YIG magnonics, J. Phys. D: Appl. Phys. **43**, 264002 (2010).

[12] A. V. Chumak, A. A. Serga, and B. Hillebrands, Magnonic crystals for data processing, J. Phys. D: Appl. Phys. **50**, 244001 (2017).

[13] M. Krawczyk and D. Grundler, Review and prospects of magnonic crystals and devices with reprogrammable band structure, J. Phys.: Condens. Matter **26**, 123202 (2014).

[14] V. V. Kruglyak, M. L. Sokolovskii, V. S. Tkachenko, and A. N. Kuchko, Spin-wave spectrum of a magnonic crystal with an isolated defect, J. Appl. Phys. **99**, 08C906 (2006).

[15] A. N. Kuchko, M. L. Sokolovskii, and V. V. Kruglyak, Spin wave spectrum of a magnonic crystal with an internally structured defect, Phys. B **370**, 73 (2005).

[16] S. A. Nikitov, P. Tailhades, and C. S. Tsai, Spin waves in periodic magnetic structures—magnonic crystals, J. Magn. Magn. Mater. **236**, 320 (2001).

[17] F. S. Ma, H. S. Lim, V. L. Zhang, S. C. Ng, and M. H. Kuok, Magnonic band structure investigation of one-dimensional bi-component magnonic crystal waveguides, Nanoscale Res. Lett. **7**, 498 (2012).

[18] C. Banerjee, S. Choudhury, J. Sinha, and A. Barman, Pseudo-one-dimensional magnonic crystals for high-frequency nanoscale devices, Phys. Rev. Appl. **8**, 014036 (2017).

[19] K. H. Chi, Y. Zhu, R. Mao, S. A. Nikitov, Y. V. Gulyaev, and C. S. Tsai, Propagation characteristics of magnetostatic volume waves in one-dimensional magnonic crystals with oblique Incidence, IEEE Trans. Magn. **47**, 3708 (2011).

[20] A. V. Chumak, A. A. Serga, B. Hillebrands, and M. P. Kostylev, Scattering of backward spin waves in a one-dimensional magnonic crystal, Appl. Phys. Lett. **93**, 022508 (2008).

[21] P. Frey, A. A. Nikitin, D. A. Bozhko, S. A. Bunyaev, G. N. Kakazei, A. B. Ustinov, B. A. Kalinikos, F. Ciubotaru, A. V. Chumak, Q. Wang, V. S. Tiberkevich, B. Hillebrands, and A. A. Serga, Reflection-less width-modulated magnonic crystal, Commun. Phys. **3**, 17 (2020).

[22] T. Goto, K. Shimada, Y. Nakamura, H. Uchida, and M. Inoue, One-dimensional magnonic crystal with Cu stripes for forward volume spin waves, Phys. Rev. Appl. **11**, 014033 (2019).

[23] M. A. Morozova, S. V. Grishin, A. V. Sadovnikov, D. V. Romanenko, Y. P. Sharaevskii, and S. A. Nikitov, Band gap control in a line-defect magnonic crystal waveguide, Appl. Phys. Lett. **107**, 242402 (2015).

[24] H. Qin, G.-J. Both, S. J. Hämäläinen, L. Yao, and S. van Dijken, Low-loss YIG-based magnonic crystals with large tunable bandgaps, Nat. Commun. **9**, 5445 (2018).

[25] Z. K. Wang, V. L. Zhang, H. S. Lim, S. C. Ng, M. H. Kuok, S. Jain, and A. O. Adeyeye, Observation of frequency band gaps in a one-dimensional nanostructured magnonic crystal, Appl. Phys. Lett. **94**, 083112 (2009).

[26] S.-K. Kim, K.-S. Lee, and D.-S. Han, A gigahertz-range spin-wave filter composed of width-modulated nanostrip magnonic-crystal waveguides, Appl. Phys. Lett. **95**, 082507 (2009).

[27] Y. Zhu, K. H. Chi, and C. S. Tsai, Magnonic crystals-based tunable microwave phase shifters, Appl. Phys. Lett. **105**, 022411 (2014).

[28] N. Kanazawa, T. Goto, and M. Inoue, Spin wave localization in one-dimensional magnonic microcavity comprising yttrium iron garnet, J. Appl. Phys. **116**, 083903 (2014).

[29] K. H. Chi, Y. Zhu, and C. S. Tsai, Two-dimensional magnonic crystal with periodic thickness variation in YIG layer for magnetostatic volume wave propagation, IEEE Trans. Magn. **49**, 1000 (2013).
[30] K. H. Chi, Y. Zhu, and C. S. Tsai, Confinement of magnetostatic forward volume waves in two-dimensional magnonic crystals with line defects, J. Appl. Phys. **115**, 17D125 (2014).
[31] S. Tacchi, G. Gubbiotti, M. Madami, and G. Carlotti, Brillouin light scattering studies of 2D magnonic crystals, J. Phys.: Condens. Matter **29**, 073001 (2017).
[32] T. Schwarze and D. Grundler, Magnonic crystal wave guide with large spin-wave propagation velocity in CoFeB, Appl. Phys. Lett. **102**, 222412 (2013).
[33] T. Schwarze, R. Huber, G. Duerr, and D. Grundler, Complete band gaps for magnetostatic forward volume waves in a two-dimensional magnonic crystal, Phys. Rev. B **85**, 134448 (2012).
[34] T. Yoshimoto, T. Goto, K. Shimada, B. Iwamoto, Y. Nakamura, H. Uchida, C. A. Ross, and M. Inoue, Static and dynamic magnetic properties of single-crystalline yttrium iron garnet films epitaxially grown on three garnet substrates, Adv. Electron. Mater. **4**, 1800106 (2018).
[35] T. Goto, Logic device using spin wave interference propagating in a magnetic insulator, Oyo Buturi **90**, 172 (2021).
[36] K. Shimada, T. Goto, N. Kanazawa, H. Takagi, Y. Nakamura, H. Uchida, and M. Inoue, Extremely flat transmission band of forward volume spin wave using gold and yttrium iron garnet, J. Phys. D: Appl. Phys. **50**, 275001 (2017).
[37] T. Weiland, Time domain electromagnetic field computation with finite difference methods, Int. J. Numer. Modell. **9**, 295 (1996).
[38] T. Weiland, M. Timm, and I. Munteanu, A practical guide to 3-D simulation, IEEE Microwave Mag. **9**, 62 (2008).
[39] K. Mori, T. Goto, T. Watanabe, T. Koguchi, Y. Nakamura, P. B. Lim, A. B. Ustinov, and M. Inoue, Broadband excitation of spin wave using microstrip line antennas for integrated magnonic devices, J. Phys. D: Appl. Phys. **55**, 115002 (2022).
[40] A. G. Gurevich and G. A. Melkov, *Magnetization Oscillations and Waves* (CRC Press, Inc, Boca Raton, 1996)
[41] R. A. Matula, Electrical resistivity of copper, gold, palladium, and silver, J. Phys. Chem. Ref. Data **8**, 1147 (1979).
[42] D. D. Stancil and A. Prabhakar, *Spin Waves* (Springer, New York, 2009)
[43] N. Kanazawa, T. Goto, J. W. Hoong, A. Buyandalai, H. Takagi, and M. Inoue, Metal thickness dependence on spin wave propagation in magnonic crystal using yttrium iron garnet, J. Appl. Phys. **117**, 17E510 (2015).
[44] See Supplemental Material at http://link.aps.org/supplemental/10.1103/PhysRevApplied.21.014061 showing other figures.
[45] M. Diem, T. Koschny, and C. M. Soukoulis, Transmission in the vicinity of the Dirac point in hexagonal photonic crystals, Phys. B **405**, 2990 (2010).
[46] S. Chakrabarti and D. Bhattacharya, Magnetostatic volume waves in lossy YIG film backed by a metal of finite conductivity, IEEE Trans. Microwave Theory Tech. **47**, 1132 (1999).
[47] J. O. Vasseur, L. Dobrzynski, B. Djafari-Rouhani, and H. Puszkarski, Magnon band structure of periodic composites, Phys. Rev. B **54**, 1043 (1996).